Acta Polytechnica **65**(1):16–24, 2025
https://doi.org/10.14311/AP.2025.65.0016

Published by the Czech Technical University in Prague

HIGH-RESOLUTION MAPPING OF SECONDARY COSMIC RAYS WITH MINIATURISED STACKED PIXEL TELESCOPE

Carlos Granja[a,b,*], Herve Chanal[c], Václav Zach[d], David Chvátil[d], Cristina Oancea[a], Dušan Poklop[b,d], Václav Olšanský[d], Jan Jakůbek[a]

[a] *Advacam, U Pergamenky 12, 170 00 Prague, Czech Republic*

[b] *VSB – Technical University of Ostrava, Faculty of Electrical Engineering and Computer Science, Department of Physics, 17. listopadu 2172/15, 708 00 Ostrava, Czech Republic*

[c] *Université Clermont Auvergne, CNRS/IN2P3, Laboratoire de Physique de Clermont-Ferrand, 4 avenue Blaise Pascal, Aubière, F-63000 Clermont-Ferrand, France*

[d] *Nuclear Physics Institute, Czech Academy of Sciences, Husinec – Řež 130, 250 68 Řež, Czech Republic*

[*] corresponding author: carlos.granja@advacam.cz

Abstract. We performed detailed measurements of the secondary cosmic ray field in the lower atmosphere (at 200 m). We use a miniaturised particle telescope consisting of two closely stacked synchronised Timepix3 detectors. Position-, spectral-, and time-sensitive particle tracking provides enhanced particle-type resolving power and high angular resolution mapping of charged particles. Evaluation and calibration of the telescope synchronised tracking and directional response was performed with proton and electron beams. The telescope architecture, modeled angular response and developed data analysis provide accurate composition characterisation and high-angular resolution directional mapping of the charged particle component. In particular, the muon component can be resolved to a high degree over the photon and electron components in the lower atmosphere. The muon angular flux is measured in a wide field of view with enhanced discrimination.

Keywords: Cosmic rays, particle tracking, radiation imaging, particle telescope, pixel detectors.

1. Introduction

Atmospheric secondary cosmic rays [1] have been the subject of studies ranging from fundamental and high-energy physics [2] to applied research such as their effects on the environment, the Earth's biosphere [3], and the atmospheric UV field and ozone composition [4]. Measurements and precise experimental data are valuable and rather scarce. Spectral and directional data are desired together with information on the composition (radiation species such as electrons, muons, X rays, gamma rays, protons, and neutrons) that are produced in broad energy and directional distributions. Studies also investigate the variability of these variables in terms of flux, altitude, and time [1].

Current experimental studies [5, 6] use complex and rather large detectors (> 1 m in size). Such systems conveniently provide high acceptance and high count rates with broad response to the charged particle field as well as gamma rays and neutrons. Drawbacks include limited angular resolution and poor detection discrimination for certain radiation components, as well as high cost and complexity for deployment, especially in remote locations, drones, and aircraft.

We aim to perform precise measurements of the composition and spectral characterisation of the secondary cosmic ray field in the lower atmosphere, in particular, in view of the muon component. We aim to achieve this with newly developed compact (hand-held size), room-temperature operated, and portable cosmic ray detection instrumentation with radiation imaging and particle tracking capabilities. Emphasis is put on high angular resolution, wide field-of-view (FoV), and enhanced discrimination to the radiation components of the secondary cosmic ray field. The trade-off is the reduced detector effective area and limited detection efficiency for the gamma-ray field due to the miniaturisation of the instrumentation. The goal is to provide a complementary high-sensitivity tool to the large-size high-efficiency systems.

For this work, we use a high-resolution miniaturised particle telescope [7] based on the semiconductor pixel detector Timepix3 [8]. The detection technique is based on the resolving power of the Timepix3 detector with extended selectivity by the telescope architecture combining timing, spectrometry (energy loss), and directional tracking response. The resolving power of particle-type classes is improved and customised for the muon component, which can be better discriminated over other components including electrons, X rays and gamma rays, which otherwise overlap in the single detector configuration.

2. Materials and instrumentation

2.1. The particle telescope MiniPIX Timepix3 1 × 2 Stack

The miniaturised particle telescope [7] consists of two MiniPIX Timepix3 cameras [9] assembled in stack configuration in close geometry (small spacing gap,

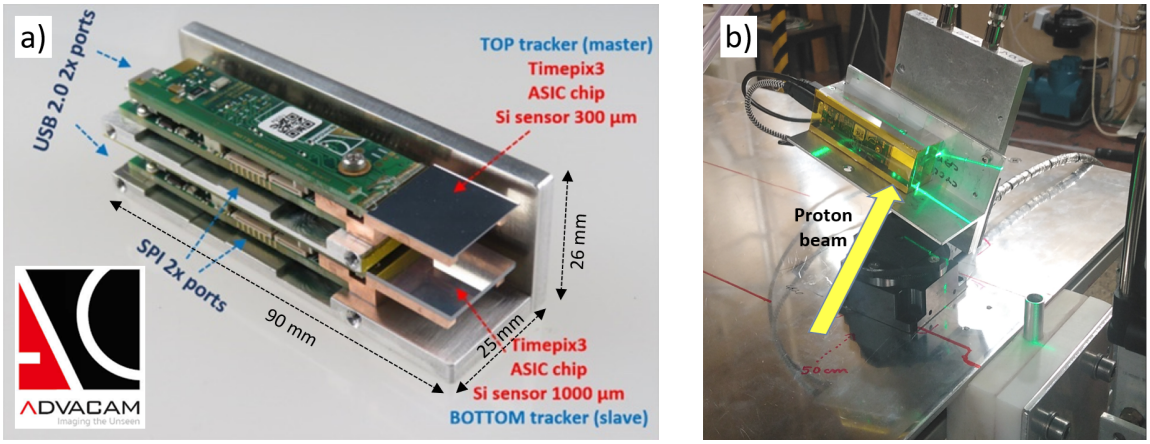

FIGURE 1. (a) The miniaturized MiniPIX Timepix3 1 × 2 Stack telescope [7] consisting of two Timepix3 pixel detectors in close assembly (10 mm spacing gap). The top tracker consists of the Timepix3 with a 300 µm silicon sensor. The bottom tracker consists of the Timepix3 with a 1 000 µm silicon sensor. (b) Measuring setup at the NPI-CAS light ion cyclotron accelerator showing the stack telescope mounted on a rotation stage and the incident proton beam.

10 mm between the pixel detectors) – see Figure 1a. It is designed to register in coincidence penetrating particles crossing both detectors.

The telescope operates at room temperature and is readout by two USB-micro cables to a standard computer running Windows or Linux. Control and data readout are performed with the PIXET software tool PIXET [10]. The raw data of the pixel detectors are stored at the computer to be processed offline.

The pixel detectors can be equipped with silicon sensors of different thicknesses – for example 300 µm and 1 000 µm for the top and bottom detectors, respectively. This configuration enables us to make use of the $\Delta E - \Delta E'$ technique for enhanced sensitivity of radiation detection and particle spectrometry (energy loss). The thinner detector is placed on top to reduce self-shielding. The ASIC chip of each Timepix3 detector is about 875 µm thick silicon, providing an additional nonsensitive volume partly shielding the bottom tracker.

2.2. Synchronised operation

The Timepix3 detectors are controlled and readout in sync. The measurement shutter open and close times for both detectors are set equal. The top tracker detector runs as the master. The bottom tracker detector runs as the slave. The detector settings at the pixel level are set to time and energy. The nominal resolution is 1.6 ns and about 5 % keV. The detectors are operated and readout at the chip level in a continuous data driven mode. The timing resolution of readout of the entire pixel matrix is at the level of 50–100 ns. Only hit pixels are readout and stored. The overall data file size is a few kB per detector per minute. Data are acquired and stored in pairs of files of 20 s of continuous measurement time. In between there is a small detector-file readout deadtime (≈ few tens of ms).

The correlated tracks of single particles crossing both detectors are simultaneously registered in wide field-of-view (FoV), nearly 60 %, with high angular resolution ($\leq 0.3°$) without the need for collimators [7].

3. Measurements

Prior to cosmic ray measurements, tests and calibration measurements were performed in well-defined radiation fields using particle accelerator beams of selected energy, fixed direction (to the detector plane) and low-intensity (< pA). The measurements were performed in air with monoenergetic proton and electron beams of size of ≈10 mm and particle flux $< 10^6$ particles $\mathrm{cm}^{-2}\,\mathrm{s}^{-1}$ at the detector position. These conditions allow for the telescope to be placed directly in the beam path (Figure 1b) and register single-particle tracks without event pile-up in the detectors [11].

The measurements at well-defined radiation fields serve to test and verify the detector count rate range as well as to examine and calibrate the telescope field-of-view, spatial and directional responses and angular resolution.

3.1. Protons

Measurements with proton beams of several beam energy and direction of incidence were performed at the U120-M light ion cyclotron of the Nuclear Physics Institute in Rez near Prague. Proton energies in the range of 8 to 33 MeV incident in various directions to the detector sensor plane, including the perpendicular direction, were studied (see Figure 2). The particles were incident from the front of the telescope arriving first at the top Timepix3 tracker with a 30 µm thick silicon sensor (Figure 2a). Penetrating energetic particles reach the bottom Timepix3 tracker with a 1 000 µm thick silicon sensor (Figure 2b).

In Figure 2, the proton tracks produce the large round clusters registered of high-energy per pixel. Unwanted and background events are also registered and

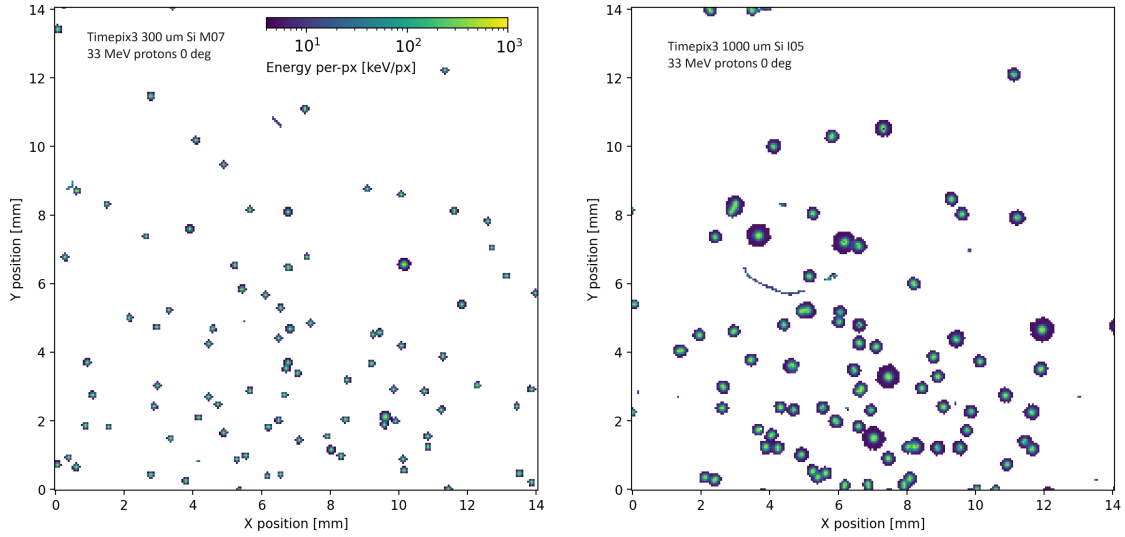

(A). Top tracker Timepix3 300 µm silicon. (B). Bottom tracker Timepix3 1 000 µm silicon.

Figure 2. Detection and track visualisation of 33 MeV protons by the stack telescope. The beam was incident perpendicular i.e., at 0° to the detector sensor plane. The figures show 100 tracks acquired in 313.6 ms and 384.2 ms, respectively. All registered particles are shown including background and unwanted events – e.g. secondary electrons and low-energy gamma rays. The full detector sensor matrix is shown (256×256 pixels $= 14.08 \times 14.08\,\mathrm{mm}^2$. The registered per-pixel deposited energy is displayed by the colour scale (in $\mathrm{keV\,px}^{-1}$).

resolved, such as X rays (small few pixel tracks) and low-energy gamma rays, which are registered via compton scattered electrons as thin curly tracks of low registered energy per-pixel. In the semiconductor sensor, the gamma rays are detected with decreasing detection efficiency as the gamma-ray energy increases [11].

In the telescope configuration used (Section 2.1), the protons registered in the bottom tracker deposite a greater energy and their tracks appear larger than in the top tracker. This is due to the lower energy of the transmitted protons, which exhibit higher energy loss (approaching the Bragg region) and also by the different sensor thickness (larger for the bottom tracker).

Information is contained also in the spatial distribution of the registered particles. In the data given in Figure 2, collected in a fraction of a second, the spatial distribution of the particle beam can be observed. This pattern becomes clearer and of higher contrast when evaluating a larger set of data. The partial shielding of the top tracker, manifested in the registered particles in the bottom tracker, is greater in the regions around the two vertical edges of the sensor (pixel columns between 0–2 mm and between 10–12 mm) due to the shielding of the chip backing holder of the top tracker (consisting of 2 mm thick Cu holder rods – seen in Figure 1a).

3.2. Electrons

Measurements were performed at the Microtron accelerator also at the NPI-CAS, Rez near Prague. Electron beams of selected energies in the range 3.8 to 22 MeV were examined at various incidence directions such as 20° as shown in Figure 3.

In the figure, all registered events consisting of the primary beam non-scattered particles (the elongated directionally oriented tracks), partly scattered electrons as well as unwanted/background events, such as X rays (small few pixel round tracks) and low-energy gamma rays (curly thin tracks of random orientation), are shown [11]. Similarly as in Figure 2, the spatial distribution of the particle beam can be observed and evaluated. A greater rate of electron beam scattered is observed, which is due to characteristic multi-scattering of electrons in the semiconductor silicon material.

3.3. Cosmic rays

Measurements of secondary cosmic rays were performed on the ground at an altitude of 200 m altitude (in Prague). Further measurements were performed also at 2.630 m (at the mountain summit Lomnicky Stit, in the Tatras mountains in Slovakia). The detection and visualisation of cosmic ray tracks are shown in Figure 4. The device was placed inside a laboratory building, where the roof partly shields low-energy particles. The telescope was placed horizontally with the top tracker facing upwards – as shown in Figure 1a. The telescope was operated in sync and readout in data driven mode in consecutive periods acquired at intervals of 20 s.

4. Particle tracking – single detector

In the first stage, data are processed separately for each pixel detector. The detailed track morphology pattern and spectral distribution of the particle tracks are analyzed as described below.

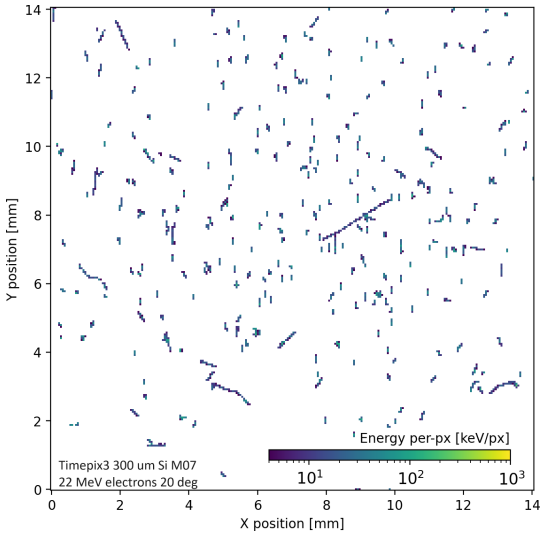

(A). Top tracker Timepix3 300 µm silicon.

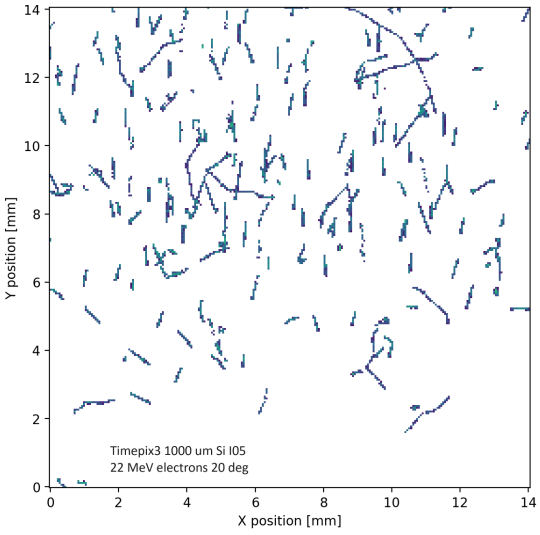

(B). Bottom tracker Timepix3 1 000 µm silicon.

FIGURE 3. Similar to Figure 2 showing the detection of 22 MeV electrons, incident at 20°, by the stack telescope. The figures show 300 tracks each, acquired in 100.7 ms and 39.7 ms, respectively.

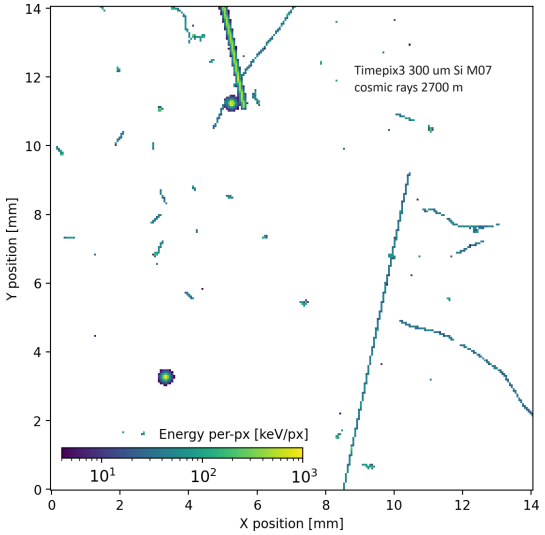

(A). Top tracker Timepix3 300 µm silicon.

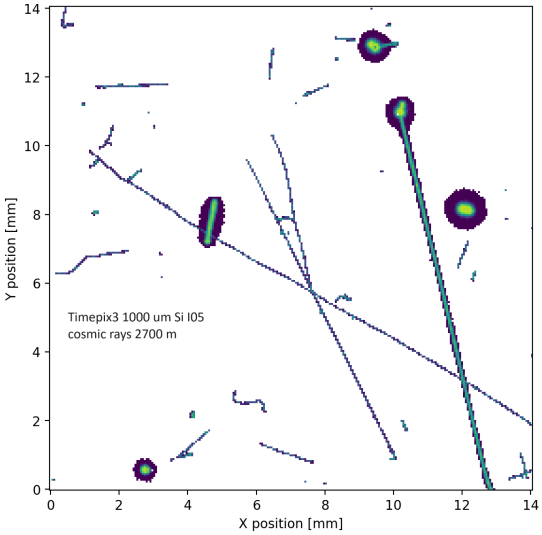

(B). Bottom tracker Timepix3 1 000 µm silicon.

FIGURE 4. Similar to Figure 2, showing the detection of secondary cosmic rays at Lomnicky Stit by the stack telescope. The figures show selected data acquired in a 60 s integrated exposure time. See text.

4.1. SINGLE PARTICLE TRACKS

On the Timepix detector, individual particles produce pixelated tracks, called *clusters* [12], which carry detailed information on the radiation. The tracks contain also any localised secondary ionisation in the detector semiconductor sensor produced by the incident particles. This is the case for the limited types and energies of the radiation in the atmosphere. Atmospheric muons and electrons, as well as residual and secondary protons produce single tracks. Eventual energetic delta electrons and reaction products in the detector sensor that produce further secondary ionization are resolved by the tracking-imaging response – see the thin overlapping tracks connected in Figure 4.

The tracks exhibit a characteristic morphology pattern and spectral-tracking response, which are determined by the degrees of freedom [11] of interaction of radiation in the Timepix detectors:

(1.) particle species,

(2.) spectral response (energy loss),

(3.) direction (to the detector sensor plane).

The detector sensor thickness and applied reversed bias also influence the sensitivity. Further information is also recorded for each track: the position of the interaction on the detector (at the pixel scale of 55 µm [12]) and the time of registration (at the ≈ 100 ns level).

The registered tracks produced are analysed by pattern recognition algorithms [13] and are compared to look-up response matrices [11, 14] produced from experimental calibrations at well-defined fields and

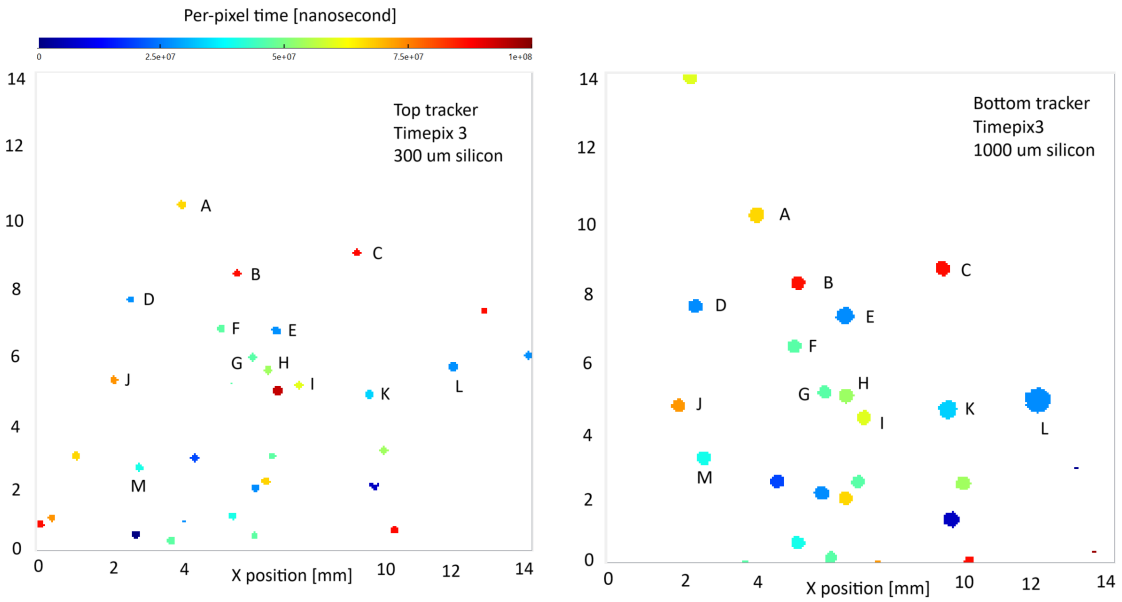

(A). Top tracker Timepix3 300 µm Si sensor.

(B). Bottom tracker Timepix3 1 000 µm Si sensor.

Figure 5. Similar to Figure 2, showing the time-correlated registration of 33 MeV protons by the stack telescope. The per-pixel time registration is displayed by the colour scale in nanoseconds. A 100 ms time interval of data is given. To aid the visual inspection, labels (capital letters – from A thru M) are added to highlight several of the coincident track pairs.

particle accelerator beams [11]. The raw data for each detector are processed with the pixel detector data processing tool DPE-TraX engine [14]. Several steps are made: identification of joint pixels forming a track cluster by a single particle (called clustering); application of the per-pixel energy calibration, derivation of the cluster centroid (or track barycentre) and directional tracking information (track length, trajectory vector in 3D – expressed by two angles: azimuth (along the sensor plane) and elevation (away from the sensor plane) angles).

4.2. Particle type classification

Analysis of the single particle tracks, together with experimental calibrations at well-defined and reference fields [11], enable to derive information on the particle-type species [11]. The resolving power by a single detector is limited to broad particle groups [11, 15]: High-energy transfer particles (HETP), which are in turn arranged into two sub-classes: protons (one class) and ions (second class). Low-energy transfer particles (LETP), which are also arranged into two sub-classes: X rays (third class) and electrons together with low-energy gamma rays (fourth class). The muons, which exhibit a similar energy loss and similar track morphology to the electrons and cannot be readily resolved in a single-chip detector, are included in the last class.

Different particle species produce different tracks of distinct and characteristic spectral-tracking morphology [11]. HETP particles produce large tracks of high per-pixel registered energy, such as the ion and proton tracks in Figure 2. LETP particles produce small and/or thin tracks of low per-pixel registered energy, such as muons and the electron tracks in Figure 3. These broad-class groups of tracks are observed in the cosmic ray data in Figure 4.

5. Particle tracking – stacked telescope

5.1. Correlated spatial detection

The selective registration of single particles in both pixel trackers is made possible by correlated spatial and time registration for both pixel detectors. The Timepix3 detectors are operated and readout in sync in a continuous data driven mode. The synchronised registration and selectivity of the technique are demonstrated in Figure 5, where the per-pixel time registration is displayed (color scale). The data interval given corresponds to a 100 ms time interval. All registered events are displayed including uncorrelated proton tracks and background events. Thus, a highly selective spatial and time correlated identification of events in both trackers by single particles can be performed.

5.2. Coincidence time window

For correlated event selection between both detectors in the telescope, the coincidence time window was evaluated – see Figure 6. A 200 ns window is set by the per-pixel time response (nominally at the *ns* level), the per-pixel time walk (up to tens of ns), and the chip-level sync readout time uncertainty in the telescope stack configuration (≈ 100 ns).

5.3. Enhanced event discrimination

The correlated detection of events in both pixel detectors enhances the resolving power and discrimination

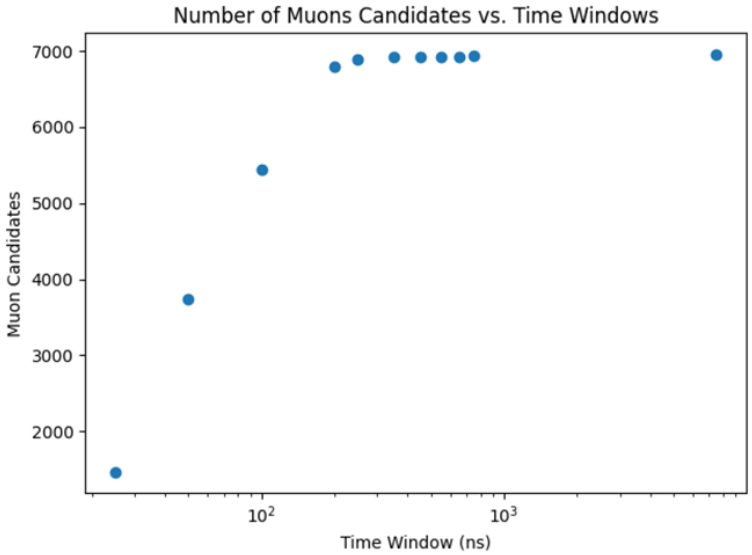

FIGURE 6. Number of detected track pairs fulfilling the filtering condition dependent on the coincidence time window. Data evaluated for cosmic ray measurements of two weeks in Prague.

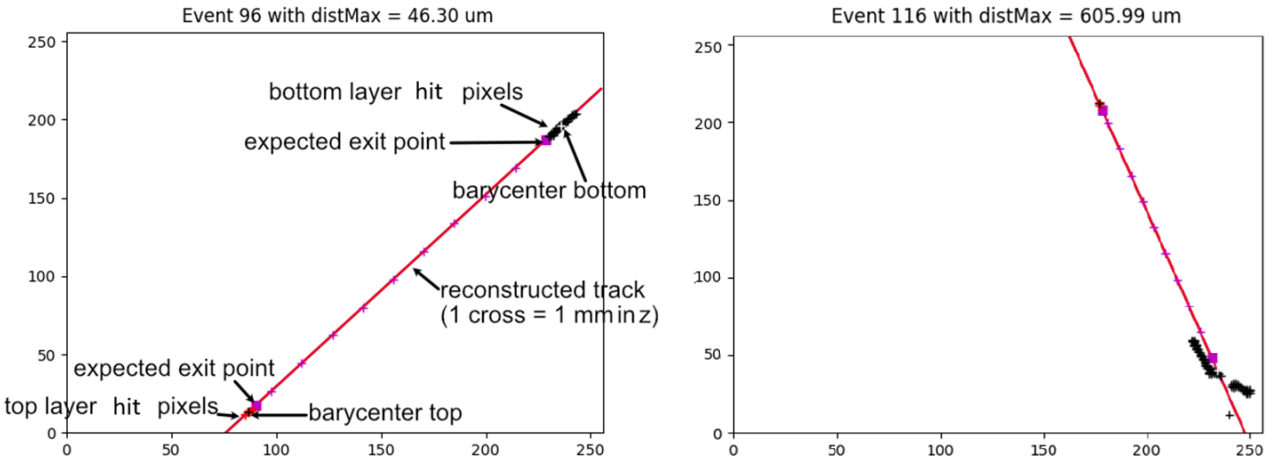

(A). Valid identification. (B). Rejected identification.

FIGURE 7. Filtering of coincidence muon events in the stack telescope by correlated tracking and projected reconstruction of directional vector for a valid, and rejected identification of coincident event pairs. The registered tracks (top detector in magenta, bottom detector in black) together with the projected trajectory (in red) for the stack spacing gap (10 mm) are displayed on the detector pixel-matrix area (256×256 pixels $= 14.08 \times 14.08\,\mathrm{mm}^2$). For muon tracks, the maximum distance (distMax) in each pixelated track is less than two pixels (110 µm).

of particle types. We combine the correlated spatial, timing, spectral (energy loss), and tracking information. The angular resolution of directional registration is also significantly improved, to sub-degree level, compared to the single particle case [16], see Section 4.

5.4. EVENT FILTERING – MUONS

Unwanted events, such as non-coincident tracks (i.e. events without a coincidence pair in the second detector), secondary, and background particles as well as random coincidences, can be recognised and filtered out. Furthermore, other unwanted coincidence events can also be partly resolved and filtered out. The muon events can be singled out to a significant extent by taking into account their characteristic energy loss and track-morphology pattern.

The muon event filtering proceeds through several conditions. The coincidence time window between the tracks of the upper and bottom detector trackers should be within 200 ns. For each set of hit pixels forming the track cluster on each pixel detector of the telescope, various steps are performed. The centroid (or barycenter) of each track is computed including the track vector entry and exit verteces. The maximum distance (called distMax) between each pixel in the given track is evaluated. If this distance is greater than 2 pixels (110 um), the event is rejected – see Figure 7.

In each of the pixelated detectors, the muons produce thin straight tracks of low energy loss. Especially at large incidence angles to the detector sensor plane, these tracks are different from tracks produced by

most atmospheric electrons, namely those of low energy (below several MeV) which exhibit similar energy loss and produce thin, but curly tracks [17]. The latter group includes events produced by low-energy gamma rays (up to a few hundred keV), which are detected with limited detection efficiency (below 0.1 %) given by the low Z-number (silicon) sensor material and small thickness.

With increasing energy, above several MeV, electrons exhibit more straight tracks that overlap those produced by muons. Such electrons can be present in the atmosphere and cannot be completely filtered out.

Protons in the lower atmosphere are essentially non-existing. For the most part, they exhibit distinct (higher) energy loss and are well-resolved up to nearly 100 MeV. Higher-energy protons, ≈ 100 MeV and above, become minimum ionising particles and exhibit lower energy loss of increasingly similar, i.e. overlapping, tracking morphology to that of muons and electrons. These events become indistinguishable.

At a small incidence direction, i.e. when the particle crosses the telescope at or near perpendicular angles, the tracking resolving power by each detector is reduced [16]. The tracks of muons and electrons become smaller and have a similar morphology (a few pixels round tracks). For muon event filtering, we interpolate the particle trajectory in the telescope between both pixel detectors and take into account the expected projected position in the second detector. With the spacing distance between the two detectors known (10 mm), the expected entry and exit points of the particle on the sensors are calculated. This provides additional filtering power associated with the procedure above. This condition is well fulfilled by muons and not for electrons – due to the characteristic multiscattering of electrons in the detector semiconductor sensor extended by the Timepix3 ASIC chip (≈ 850 µm thick silicon). The probability of atmospheric electrons to produce thin tracks on both detectors, which are moreover aligned along a straight directional vector, is very small. This is also the case with background and other secondary particles.

5.5. Field of view, angular resolution

The pixelated clusters in each detector tracker are spatially determined at the pixel level even with subpixel resolution [12, 18]. The correlated vertex entry and exit points make it possible to reconstruct the particle trajectory in 3D with high spatial (µm level) and high angular resolution ($\leq 0.3°$). In the telescope configuration, the field of view for the reconstruction of coincident events is 60 % with an elevation pitch angle of $\theta = 54°$ from the perpendicular zenith direction. These values are determined by the telescope spacing gap (10 mm). The resulting spatial vector visualisation of discriminated muon trajectories is given in Figure 8. In the figure, the projected view along the vertical plane is shown.

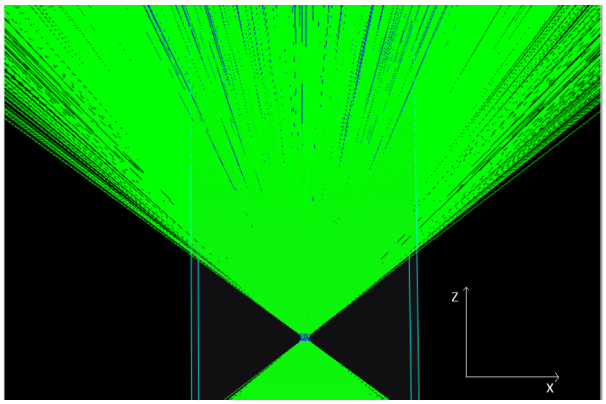

Figure 8. Visualisation of spatial trajectory of registered coincidence muons. The figure shows the projected trajectories on the vertical plane XZ to the telescope horizontal plane XY.

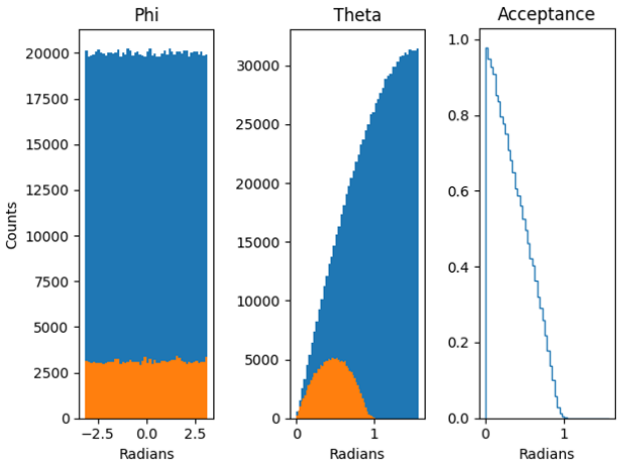

(a). ϕ. (b). θ. (c). Acceptance.

Figure 9. Monte-Carlo simulated muon events in the telescope along the azimuth ϕ and elevation θ directions. Only part of the generated events (blue) are accepted (orange). Resulting telescope angular acceptance w dependence on elevation angle θ.

5.6. Angular flux, geometrical acceptance

The angular dependence of the particle flux on the elevation i.e. zenith angle θ, is derived as:

$$I(\theta) = I_0 \cos^n(\theta)\,\mathrm{cm}^{-2}\,\mathrm{s}^{-1}\,\mathrm{sr}^{-1}, \qquad (1)$$

where I_0 is the maximum flux and $n = 2$ in first approximation [19].

To determine the geometrical acceptance, we chose to use a Monte-Carlo approach. We simulated a large set of muons generated evenly on a half sphere around the telescope. We count the events which cross the two pixel detectors to derive the acceptance (blue generated, orange accepted) – see Figure 9. The numerical simulation of the acceptance serves to derive the different weight applied to the measured data.

The model above is derived in spherical coordinates. In order to express it in steradians, we make use of

the Lefevre equation, which is basically a modification of the Jacobian for the solid angle:

$$d\Omega = \sin(\theta)\, d\theta d\phi. \tag{2}$$

Integrating with a binned approach, it becomes:

$$\Delta\Omega = 2\pi(\cos(\theta_0) - \cos(\theta_0 + \Delta\theta)). \tag{3}$$

With the following variable change, thereby moving to a variable bin size:

$$\theta' = \arccos\left(\frac{\theta}{2\pi}\right), \tag{4}$$

it leads to:

$$\Delta\Omega = \Delta\theta'. \tag{5}$$

We generate the events on a semi-sphere and compare the detection ratio between our detector and a perfect system. The difference lies in the angular binning. The simulated events are sampled using the same binning as the acquired data giving the angular acceptance $w(\Delta\theta_i)$ for each $\Delta\theta_i$ bin. The angular bins are derived from Equation (5), leading to a non-linear $\Delta\theta_i$ bin size.

5.7. Muon flux

For the data, we use the same variable bins derived from the Lefevre's equation used in the model to count the number of muon candidates per unit of solid angle $N_{\text{exp}}(\theta')$. The number of muons in each bin reconstructed from the data $e(\Delta\theta_i)$ is counted. The muon angular distribution is derived as $e(\Delta\theta_i) \cdot w(\Delta\theta_i)^{-1}$.

The resulting directional distribution is given in Figure 10, which is obtained from two weeks of data at an elevation of 200 m. The experimental data are fitted to a model estimation [1].

6. Conclusion

The stack telescope architecture, together with the high spatial granularity, per-pixel spectral, and time response of Timepix3 [8] are combined to characterise and measure in detail the secondary cosmic ray field in the atmosphere. Exploiting the characteristic energy loss, tracking, and morphology information on the single particle tracks at the micro-scale level, the muon component is selectively resolved with enhanced discrimination. An admixture of high-energy electrons, above several MeV, cannot be excluded. Detailed angular flux of the muon component is produced in a relatively wide field of view (nearly 60 %) of the full FoV with high angular resolution ($\leq 0.3°$).

The next steps consist of processing the cosmic ray data acquired in longer periods and high-altitude measurements at mountain summits. Future work includes adjusting the methodology and data processing of cosmic ray data acquired by a similar telescope in different configuration: closer geometry (4 mm spacing gap) and different sensor configuration (500 µm silicon for the top tracker and 2 000 µm CdTe for the bottom tracker).

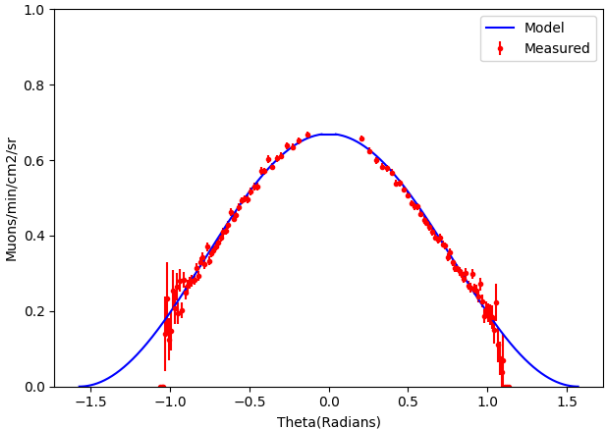

Figure 10. Muon angular flux. Evaluated from two weeks of cosmic ray data collected at 200 m altitude in Prague.

Acknowledgements

This work has been performed in frame of the project 21GRD02 BIOSPHERE with funding from the European Partnership on Metrology, co-financed from the European Union's Horizon Europe Research and Innovation Programme and by the Participating States. Work at VSB TU Ostrava was supported by the project SGS SP 2024/016 at the VSB Ostrava financed by the Ministry of Education, Youth and Sports of the Czech Republic.

References

[1] L. I. Dorman. *Cosmic rays in the Earth's atmosphere and underground*. Springer, New York, USA, 2004. https://doi.org/10.1007/978-1-4020-2113-8

[2] A. Merlot, A. J. Krejci, B. C. Thomas, et al. Atmospheric consequences of cosmic-ray variability in the extragalactic shock model. *Journal of Geophysical Research: Planets* **113**:E10007, 2008. https://doi.org/10.1029/2008JE003206

[3] D. Atri, A. L. Melott. Cosmic rays and terrestrial life: A brief review. *Astroparticle physics* **53**:186–190, 2014. https://doi.org/10.1016/j.astropartphys.2013.03.001

[4] L. O. Bjorn, R. L. McKenzie. *Photobiology: The Science of Life and Light*, chap. Ozone depletion and the effects of ultraviolet radiation. Springer, New York, USA, 2008. https://doi.org/10.1007/978-0-387-72655-7_19

[5] M. Rockenbach, A. D. Lago, N. J. Schuch, et al. Global muon detector network used for space weather applications. *Space Science Review* **182**(1):1–18, 2014. https://doi.org/10.1007/s11214-014-0048-4

[6] A. Chilingarian, G. Hovsepyan, K. Arakelyan, et al. Space environmental viewing and analysis network (SEVAN). *Earth, Moon, and Planets* **104**(1):195–210, 2009. https://doi.org/10.1007/s11038-008-9288-1

[7] C. Granja, J. Jakubek, P. Soukup, et al. Spectral tracking of energetic charged particles in wide field-of-view with miniaturized telescope MiniPIX Timepix3 1 × 2 stack. *Journal of Instrumentation* **17**:C03028, 2022. https://doi.org/10.1088/1748-0221/17/03/C03028

[8] T. Poikela, J. Plosila, T. Westerlund, et al. Timepix3: a 65K channel hybrid pixel readout chip with simultaneous ToA/ToT and sparse readout. *Journal of Instrumentation* **9**:C05013, 2014. https://doi.org/10.1088/1748-0221/9/05/C05013

[9] C. Granja, J. Jakubek, P. Soukup, et al. MiniPIX Timepix3 – a miniaturized radiation camera with onboard data processing for online characterization of wide-intensity mixed-radiation fields. *Journal of Instrumentation* **17**:C03019, 2022. https://doi.org/10.1088/1748-0221/17/03/C03019

[10] Advacam. *PIXET software tool for operation and readout of pixel detectors Timepix/Medipix*, 2015.

[11] C. Granja, J. Jakubek, S. Polansky, et al. Resolving power of pixel detector Timepix for wide-range electron, proton and ion detection. *Nuclear Instruments and Methods in Physics Research Section A: Accelerators, Spectrometers, Detectors and Associated Equipment* **908**:60–71, 2018. https://doi.org/10.1016/j.nima.2018.08.014

[12] J. Jakubek, A. Cejnarova, T. Holy, et al. Pixel detectors for imaging with heavy charged particles. *Nuclear Instruments and Methods in Physics Research Section A: Accelerators, Spectrometers, Detectors and Associated Equipment* **591**(1):155–158, 2008. https://doi.org/10.1016/j.nima.2008.03.091

[13] T. Holy, E. Heijne, J. Jakubek, et al. Pattern recognition of tracks induced by individual quanta of ionizing radiation in Medipix2 silicon detector. *Nuclear Instruments and Methods in Physics Research Section A: Accelerators, Spectrometers, Detectors and Associated Equipment* **591**(1):287–290, 2008. https://doi.org/10.1016/j.nima.2008.03.074

[14] L. Marek, C. Granja, J. Jakubek, et al. Data processing engine (DPE): Data analysis tool for particle tracking and mixed radiation field characterization with pixel detectors Timepix. *Journal of Instrumentation* **19**:C04026, 2024. https://doi.org/10.1088/1748-0221/19/04/C04026

[15] C. Granja, J. Solc, J. Gajewski, et al. Composition and spectral characterization of mixed-radiation fields with enhanced discrimination by quantum imaging detection. *IEEE Transactions on Nuclear Science* **71**(4):921–931, 2024. https://doi.org/10.1109/TNS.2024.3369972

[16] C. Granja, K. Kudela, J. Jakubek, et al. Directional detection of charged particles and cosmic rays with the miniaturized radiation camera MiniPIX Timepix. *Nuclear Instruments and Methods in Physics Research Section A: Accelerators, Spectrometers, Detectors and Associated Equipment* **911**:142–152, 2018. https://doi.org/10.1016/j.nima.2018.09.140

[17] C. Granja, P. Krist, D. Chvatil, et al. Energy loss and online directional track visualization of fast electrons with the pixel detector Timepix. *Rad Measurements* **59**:245–261, 2013. https://doi.org/10.1016/j.radmeas.2013.07.006

[18] B. Bergmann, T. Billoud, P. Burian, et al. Particle tracking and radiation field characterization with Timepix3 in ATLAS. *Nuclear Instruments and Methods in Physics Research Section A: Accelerators, Spectrometers, Detectors and Associated Equipment* **978**:164401, 2020. https://doi.org/10.1016/j.nima.2020.164401

[19] J. Beringer, J. F. Arguin, R. M. Barnett, et al. Review of particle physics. *Physical Review D* **86**:010001, 2012. https://doi.org/10.1103/PhysRevD.86.010001